Chemical Engineering Journal 525 (2025) 170580

Contents lists available at ScienceDirect

Chemical Engineering Journal

journal homepage: www.elsevier.com/locate/cej

Acetic acid-assisted synthesis of Zr-based metal organic framework for rapid and efficient low-concentration ammonia adsorption

Jia-Hui Chen [a,1], Hao-Yu Jiang [a,1], Wen-Qiang Gong [b], Wei Hui [a], Xiao-Liang Zhang [a], Ming-Shuai Sun [a], Jia-Yin Zhang [a], Dan-Dan Cai [a,*], Duan-Jian Tao [a,*]

[a] School of Chemical Engineering, Key Laboratory of Fluorine and Silicon for Energy Materials and Chemistry of Ministry of Education, Jiangxi Normal University, Nanchang, 330022, PR China

[b] School of Chemistry and Food Science, Nanchang Normal University, Nanchang, 330032, PR China

ARTICLE INFO

Keywords:
Metal-organic framework
Acid-assisted
Adsorption
Separation
Low-concentration ammonia

ABSTRACT

Metal-organic frameworks (MOFs) have been acclaimed as potential adsorbents for gas separation, yet their intrinsic microporosity and site-saturated coordination often lead to slow adsorption kinetics and poor selectivity under low-concentration gas conditions. To address this challenge, we developed an acetic acid-assisted synthesis strategy to engineer Zr-based MOFs (UiO-66-V, V = acetic acid volume) with enhanced Lewis acids sites and porous structure. The optimal UiO-66-2.5 variant achieves an adsorption rate six times higher than that of pristine UiO-66 and superior ideal adsorption solution theory selectivities for 3 % NH_3/97 % N_2 (745) and 3 % NH_3/97 % H_2 (6036) at 298.2 K and 1.0 bar. Dynamic breakthrough experiments confirm the excellent regenerative stability and separation performance of UiO-66-2.5, achieving a retention time of 120 min g^{-1} for a simulated industrial gas mixture (3 % NH_3/24.25 % N_2/72.75 % H_2), outperforming pristine UiO-66 (84 min g^{-1}). Furthermore, the optimized 90 % UiO-66-2.5@PVA pellets exhibit a breakthrough time of 100 min·g^{-1}, which is comparable to that of the UiO-66-2.5 powder. Moreover, UiO-66-2.5 could maintain 92 % capacity over 10 adsorption-regeneration cycles. Comprehensive characterization studies revealed that the enhanced NH_3 uptake and separation performance originate from the higher surface areas and increased Lewis acids sites in UiO-66-2.5 compared to the pristine material. This work establishes acid-assisted synthesis as an effective strategy for designing MOFs that meet the capacity, kinetics, and stability requirements for industrial NH_3 capture.

1. Introduction

Ammonia (NH_3) serves as a vital industrial feedstock with widespread applications in agriculture, chemical manufacturing, and pharmaceutical industries [1,2]. Also, NH_3 has emerged as a promising carbon-free energy carrier for renewable energy systems due to its high hydrogen density and favorable liquefaction properties [3]. To meet the demand, over 150 million tons of NH_3 are synthesized annually via the well-known Haber-Bosch process using N_2 and H_2 feedstocks. However, vapor-liquid equilibrium limitations in this process result in approximately 3 % of produced NH_3 remaining unliquefied, which not only reduces N_2 and H_2 conversion efficiency in the synthesis loop but also necessitates costly gas recirculation [4–7]. Besides, the NH_3 emissions present substantial environmental and health hazards owing to their inherent toxicity and corrosiveness [8]. To mitigate these problems, adsorption technology is widely used as a promising approach for the economic and efficient removal of low-concentration NH_3 from industrial emissions [9,10]. Therefore, the development of advanced adsorbents is an urgent need for efficient low-concentration NH_3 adsorption and controlled release in industrial synthetic ammonia recycle gas.

Metal organic frameworks (MOFs) have emerged as promising candidates for NH_3 adsorption and separation due to their ultrahigh specific surface areas, tunable metal sites, and adjustable pore size [11–14]. For instance, Jeffrey R. Long's group demonstrated the potential of MOFs for reversible NH_3 storage through a unique cooperative insertion mechanism, where NH_3 molecules sequentially coordinate to metal-carboxylate bonds to form stable 1D polymeric chains [12]. Although MOFs could achieve exceptional NH_3 adsorption capabilities, the strong

* Corresponding authors.
E-mail addresses: caidd@jxnu.edu.cn (D.-D. Cai), djtao@jxnu.edu.cn (D.-J. Tao).
[1] These authors contributed equally to this work.

https://doi.org/10.1016/j.cej.2025.170580
Received 16 September 2025; Received in revised form 4 November 2025; Accepted 5 November 2025
Available online 9 November 2025

Lewis acid-base interaction between NH_3 and often triggers irreversible structural collapse during cyclic operations [15–18]. Recently, strategic selection of metal nodes (such as Al, Zr, Cr) with relatively inert nature has proven effective in balancing adsorption affinity with framework stability. Among these, Zr-based MOFs have emerged as particularly promising candidates due to the high oxophilicity and flexible coordination geometry of Zr^{4+} nodes, which exhibit sufficient NH_3 binding energy while maintaining structural integrity [19–23]. For example, defect-engineered Cu(I/II) sites achieve remarkable reversible uptake of 11.8 mmol g^{-1} at 273 K and 1.0 bar [24]. Despite these advantages, existing Zr-MOF adsorbents still face challenges, including complex synthesis, low yield, slow adsorption rates and limited selectivity of low-concentration NH_3, hindering their application in synthetic ammonia recycle gas. Therefore, developing a simple and flexible strategy to improve low-concentration NH_3 adsorption and separation performance in Zr-MOFs remains a critical challenge.

Acid-assisted synthesis provides a versatile strategy for precisely engineering defects and optimizing the structural and functional properties of MOFs [25–29]. By carefully regulating the acid concentration during synthesis, coordinatively unsaturated Zr sites can be selectively introduced, generating accessible open metal sites that significantly enhance NH_3 adsorption capacity [23,28–30]. Among various acid modulators, acetic acid stands out due to its moderate coordinating strength, steric hindrance from the methyl group, and suitable pKa value. These features collectively facilitate precise control over the crystallization process and defect architecture in UiO-66, yielding optimized crystallinity, tailored surface properties, and improved stability for enhanced NH_3 uptake [26,31,32]. However, the structural and adsorptive properties of Zr-MOFs exhibit a pronounced dependence on acid concentration, where optimal loading enhances framework regularity and creates tailored defects, whereas excessive acid results in linker displacement and pore collapse [20,33]. Moreover, although many powdered adsorbents exhibit promising performance under idealized laboratory conditions, such environments often differ substantially from those in real industrial gas separation systems [34,35]. Therefore, to bridge this gap, adsorbents must be shaped into robust structured bodies such as pellets, extrudates or composite membranes. In particular, extrusion pelletization offers notable advantages including high mechanical strength, low solvent consumption, operational simplicity, and scalability [5,6]. Thus, pelletizing Zr-MOF powders with suitable binders represents a viable pathway for balancing high adsorption capacity, mechanical robustness, and industrial processability, paving the way for more efficient NH_3 separation from industrial NH_3 recycle gas.

Herein, we successfully synthesized a series of Zr-MOFs denoted as UiO-66-V (where V represents the volume of acetic acid) to systematically tailor their textural properties and surface chemistry for enhanced low-concentration NH_3 capture. By precisely controlling acetic acid concentration, the specific surface area and the density of Lewis acid sites were simultaneously optimized, thereby effectively modulating the host-guest interactions between NH_3 molecules and Zr-based nodes. Comprehensive characterization (including XRD, N_2 physisorption, XPS, and FTIR spectroscopy) confirmed the preservation of crystallinity while revealing enhanced porosity and tailored surface functionality. As expected, the UiO-66-2.5 showed highly efficient low-concentration NH_3 capture. Furthermore, we established structure-property relationships through thermodynamic analysis of temperature-dependent adsorption isotherms. Finally, the NH_3 column breakthrough tests and recycling experiments were conducted to validate the separation performance and reusability of UiO-66-2.5 for ammonia recovery applications. The pelleted UiO-66-2.5 adsorbent was subjected to low-concentration NH_3 breakthrough tests and mechanical wear testing to evaluate its industrial applicability.

2. Experimental section

2.1. Materials

Zirconium(IV) chloride ($ZrCl_4$, 99.9 %) was provided by Shanghai Macklin Biochemical Co., Ltd. Benzene-1,4-dicarboxylic acid (BDC, 99 %), methanol (99.8 %), *N*,*N*-dimethylformamide (DMF, 99.5 %), polyvinyl alcohol (PVA, AR) and carboxymethyl cellulose (CMC, AR) were purchased from Shanghai Aladdin Biochemical Technology Co., Ltd. Acetic acid (HAc, 99.8 %) was obtained from Shanghai Titan Scientific Co., Ltd. Hydroxyethyl cellulose (HEC, AR) was acquired from Shanghai Macklin Biochemical Co., Ltd. Gases including ammonia (NH_3, 99.99 %), nitrogen (N_2, 99.99 %), and hydrogen (H_2, 99.99 %) were supplied by Jiangxi Huahong Special Gas Co., Ltd. All experimental reagents and solvents were used as received without further purification.

2.2. Synthesis of UiO-66 and UiO-66-V (V = 1.0, 2.5, 4.0)

A series of UiO-66-V materials were synthesized according to a previously reported method with slight modifications [36]. First, 0.2330 g of $ZrCl_4$ and 0.1661 g of BDC ligand in the molar ratio (1:1) were added to 30 mL of DMF and dissolved by sonication. Then, 2.5 mL of HAc was slowly added into the above mixture under the stirring conditions to form the homogeneous solution. Subsequently, the above solution was transferred to a 50 mL Teflon-lined autoclave, which was maintained in an oven at 120 °C for 24 h. After cooling naturally to room temperature, the white precipitates were collected by centrifugation and washed thoroughly with DMF and methanol at least three times. The collected solid was immersed in methanol overnight at room temperature. Finally, the product was centrifuged, dried in a vacuum oven at 80 °C for 12 h and denoted as UiO-66-V (V = 2.5).

Besides, the synthesis method of UiO-66, UiO-66-1.0 and UiO-66-4.0 was similar to that of UiO-66-2.5, except for the use of different volumes of the HAc (0, 1.0, 4.0 mL, respectively).

2.3. Preparation of UiO-66-2.5 pellets

Pelletized composites containing UiO-66-2.5 were prepared using PVA, CMC, and HEC as binders, following a consistent procedure across all samples. A representative synthesis for 90 % UiO-66-2.5@PVA is described as follows: 0.9 g of UiO-66-2.5 powder was thoroughly mixed with 0.1 g of a 10 wt% aqueous PVA solution in a mortar. The resulting moist mixture was then shaped into pellets approximately 2 mm in diameter using a pelletizing mold. The final white pellets were dried in a vacuum oven at 80 °C for 12 h and designated as 90 % UiO-66-2.5@PVA. The 90 % UiO-66-2.5@HEC and 90 % UiO-66-2.5@CMC samples were fabricated following the same protocol, with the only difference being the type of binder used.

2.4. Gas adsorption experiments

The NH_3 adsorption performances of UiO-66-V were evaluated by using a custom-built adsorption apparatus at different temperatures and pressures (Fig. S1) [37]. For the desorption and regeneration, the NH_3-loaded sample was placed in a stainless vacuum tank at 80 °C and 0.1 kPa for 2 h, then cooled down to 25 °C for the subsequent cyclic adsorption tests.

2.5. Breakthrough tests

Dynamic breakthrough experiments for NH_3 were carried out using a Micromeritics AutoChem II 2920 at 303.2 K and 1 bar. A feed gas mixture of 3 % NH_3/24.25 % N_2/72.75 % H_2 was introduced at a flow rate of 25 mL min^{-1} controlled by a mass flow controller. The effluent composition was monitored by mass spectrometry (HIDEN DECRA) (Fig. S2). Desorption process is accomplished by programmed

temperature elevation inside the instrument and the heating rate is 10 °C min^{-1}, accompanied by He flowing for 30 min. All measured data are averages of three independent measurements to ensure their accuracy and reproducibility.

3. Results and discussion

3.1. Preparation and characterization of adsorbents

Fig. 1a schematically illustrates the synthesis of UiO-66-V. The adsorbent was synthesized via a one-step solvothermal method using $ZrCl_4$ as the metal source, benzene-1,4-dicarboxylic acid (BDC) as the organic linker, and acetic acid (HAc) as aid. To determine the crystal structures, X-ray diffraction (XRD) analysis was performed on UiO-66 and UiO-66-V (V = 1.0, 2.5, 4.0). As shown in Fig. 1b, the characteristic diffraction peak at 7.52°, 8.68°, and 25.88° corresponds to the (111), (002), (006) crystallographic planes of the simulated UiO-66 (CCDC: 2054314) [38], respectively, confirming successful synthesis of the target Zr-MOF. More interestingly, the (111) peak of UiO-66-2.5 exhibits a significant low-angle shift compared to that of pristine UiO-66. According to the Bragg's law, the crystal spacings of UiO-66-2.5 are 1.213 nm, which is larger than that (1.175 nm) of UiO-66 and simulated UiO-66 (1.199 nm).

As depicted in Fig. 1c, the characteristic peaks of UiO-66 are observed at 1581 cm^{-1} and 1405 cm^{-1}, which correspond to the asymmetric and symmetric stretching vibrations of the carboxylate group (COO^-), respectively [39]. Notably, the asymmetric COO^- stretching vibration in UiO-66-2.5 appears at 1587 cm^{-1}, exhibiting a distinct high-frequency shift compared to that of pristine UiO-66 (1581 cm^{-1}). The shift suggests an enhanced electron density withdrawal from the carboxylate group, likely resulting from strengthened coordination between the C═O group and the Zr sites. In contrast to the free BDC ligand, where the corresponding peaks are located at 1714 cm^{-1} and 1450 cm^{-1}, the significant low-frequency shifts of these COO^- vibrations further confirm successful coordination to the Zr nodes. Moreover, a new peak emerges at 669 cm^{-1} in UiO-66, which is attributed to Zr—O stretching vibrations, providing additional evidence for the successful synthesis of the Zr-based MOF [40].

To further investigate the morphology and structural characteristics of the UiO-66-V, scanning electron microscope (SEM) and transmission electron microscopy (TEM) were conducted. UiO-66-2.5 exhibits a regular octahedral shape with uniform particle sizes of approximately 150 nm (Fig. 2a and b). Besides, UiO-66-1.0 and UiO-66-4.0 (Fig. S3a and b) display more well-defined crystal shapes compared to pristine UiO-66 (Fig. 2d and e). The results show that the volume of HAc significantly influences the material's morphology [25]. The high-resolution TEM (HRTEM) images (Fig. 2c and f) reveal distinct lattice fringes with an interplanar spacing of 0.299 nm, corresponding to the (444) crystal plane of UiO-66-2.5, which is consistent with the XRD analysis. The interplanar spacing of UiO-66-2.5 shows a slight expansion relative to that of UiO-66 (0.296 nm). High-angle annular dark-field scanning transmission electron microscopy (HAADF-STEM) image and energy-dispersive X-ray spectroscopy (EDS) mapping results (Fig. 2g–j) confirm the homogeneous distribution of zirconium (Zr), oxygen (O), and carbon (C) throughout the UiO-66-2.5 nanoparticles, affirming the structural integrity of the material.

To demonstrate the effect of HAc addition on the specific surface area and porosity of the UiO-66-V, N_2 adsorption-desorption experiments were carried out at 77 K. The specific surface area was calculated using the Brunauer-Emmett-Teller (BET) model. As shown in Fig. 3a, the

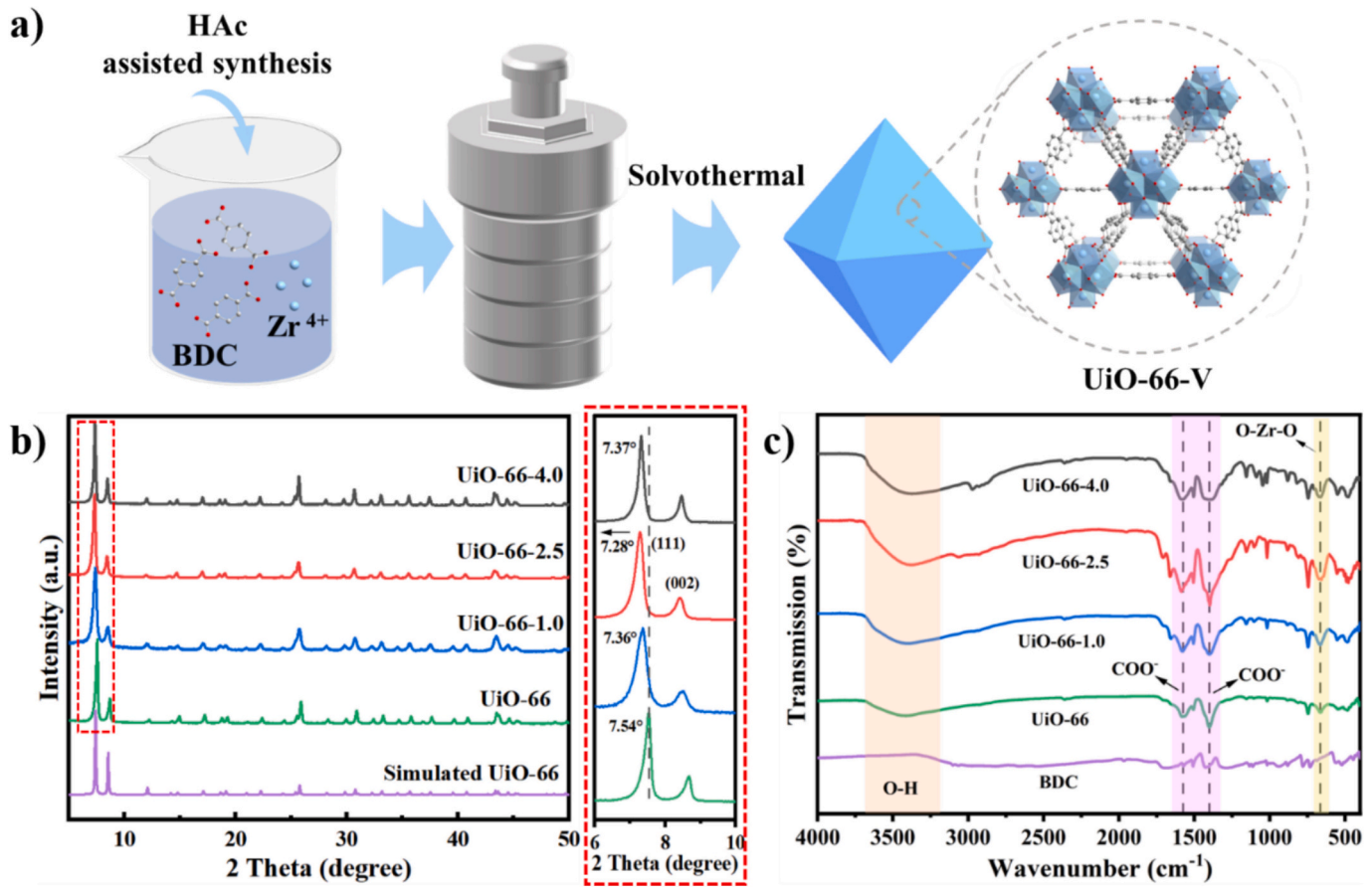

Fig. 1. (a) Schematic illustration of the synthesis of UiO-66-V (V = 1.0, 2.5, 4.0), (b) XRD patterns and (c) Fourier transform infrared (FTIR) spectra of the simulated UiO-66, pristine UiO-66, UiO-66-V and BDC.

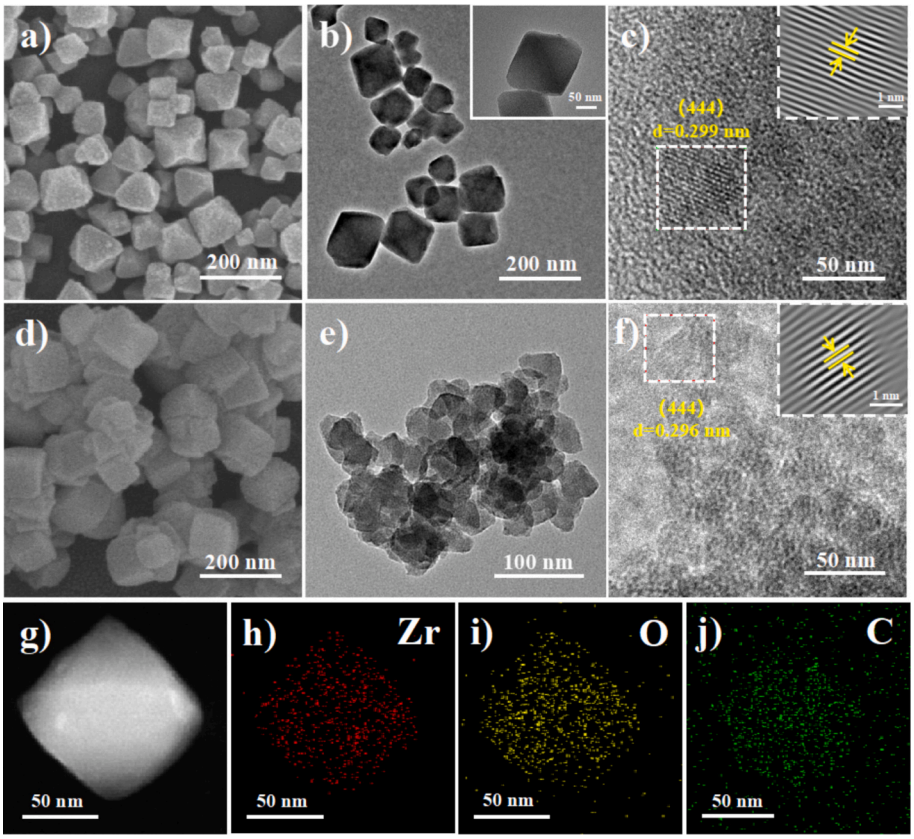

Fig. 2. (a) SEM, (b) TEM, (c) HRTEM images of UiO-66-2.5, (d) SEM, (e) TEM, (f) HRTEM images of UiO-66 (g) HAADF-STEM image and (h–j) corresponding EDS mapping of UiO-66-2.5 (red stands for Zr, yellow for O and green for C).

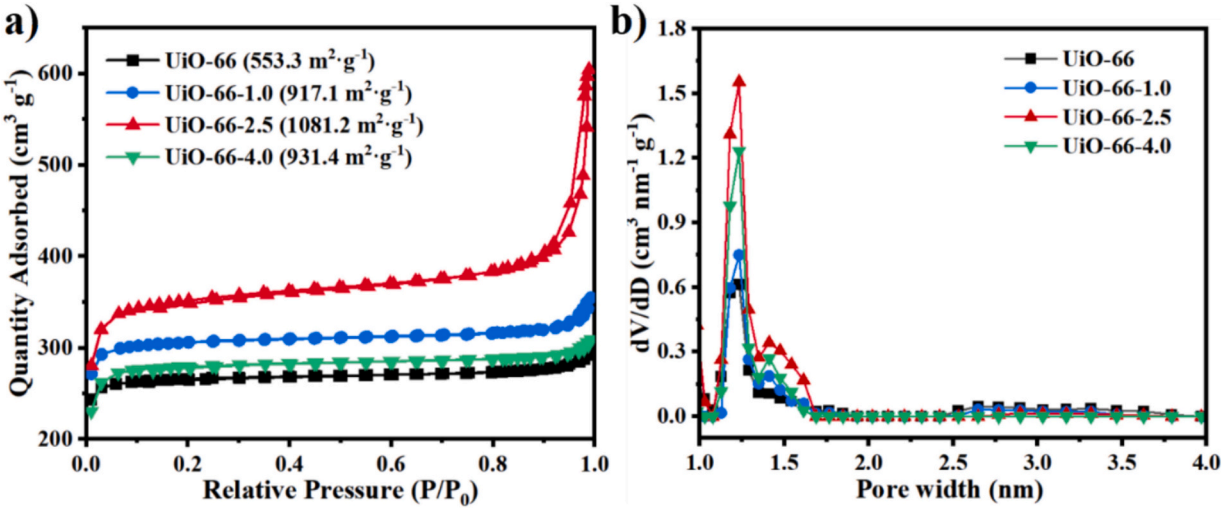

Fig. 3. (a) N_2 adsorption-desorption isotherms and (b) pore size distribution diagrams of UiO-66 and UiO-66-V (V = 1.0, 2.5, 4.0) derived from non-local density functional theory (NLDFT) analysis.

adsorption-desorption isotherms of UiO-66-V exhibit Type IV characteristics with an H4 hysteresis loop [20,41,42]. Among all variants, UiO-66-2.5 demonstrates the higher BET surface area of 1081.2 $m^2\ g^{-1}$, compared to 917.1 $m^2\ g^{-1}$ for UiO-66-1.0, 931.4 $m^2\ g^{-1}$ for UiO-66-4.0, and 553.3 $m^2\ g^{-1}$ for pristine UiO-66 (Table S1). The larger specific surface area likely facilitates the exposure of more adsorption sites, thereby enhancing NH_3 adsorption performance [23]. The pore size distribution derived from non-local density functional theory (NLDFT) analysis (Fig. 3b) indicates that both pristine UiO-66 and UiO-66-V variants exhibit a primary micropore size of approximately 1.25 nm. Notably, UiO-66-2.5 displays a distinctly enhanced volume of larger micropores centered around 1.41 nm. Given that the kinetic diameter of NH_3 is about 0.37 nm, these expanded micropores serve as efficient transport pathways, significantly reducing diffusion resistance and improving accessibility of NH_3 molecules to the internal porous network. In parallel, t-plot analysis of the N_2 sorption isotherms (Fig. S4) reveals that UiO-66-2.5 exhibits a larger micropore volume of 0.514 $cm^3 \cdot g^{-1}$ than that (0.196 $cm^3 \cdot g^{-1}$) of pristine UiO-66. Therefore, these

results suggest that UiO-66-2.5 possesses not only a higher specific surface area but also a more optimized pore structure, which collectively contribute to its superior NH_3 adsorption capacity and faster adsorption kinetics.

The surface composition and chemical states of pristine UiO-66 and UiO-66-V were investigated by X-ray photoelectron spectroscopy (XPS). Survey spectra (Fig. S5) confirmed the presence of C, Zr, and O on the surfaces of both materials. All binding energies were referenced to the C 1s peak set at 284.80 eV. As shown in the deconvoluted C 1s spectra (Fig. 4a), the peaks located at 284.80 eV, 286.49 eV, and 288.76 eV are attributed to C═C, C—C, and C═O species, respectively. In the high-resolution Zr 3d spectrum of UiO-66 (Fig. 4b), the peaks located at 182.82 eV and 185.21 eV correspond to Zr $3d_{5/2}$ and Zr $3d_{3/2}$ of Zr^{4+} species. Notably, a consistent shift of approximately 0.1 eV toward higher binding energy is observed in UiO-66-2.5 compared to the pristine sample, indicating reduced electron density around the Zr centers and enhanced Lewis acidity [43]. This suggests successful modulation of the electronic environment of Zr through HAc assistance. The O 1s spectra of UiO-66 (Fig. 4c) can be fitted with three components of C—O (533.21 eV), C═O (531.73 eV), and Zr—O (530.30 eV). In contrast, the corresponding peaks in UiO-66-2.5 shift by approximately 0.1 eV toward higher binding energies, suggesting electron withdrawal from oxygen atoms toward the carboxylate-Zr coordination sites [44]. To quantify the defect density, the BDC/Zr molar ratio was estimated from TGA (Fig. 4d). The smaller weight loss associated with framework collapse in UiO-66-2.5 compared to pristine UiO-66 indicates a higher concentration of missing-linker defects in the acetic acid-assisted sample [26]. These results confirm that the assisted synthesis successfully introduces structural defects and hierarchical porosity, which synergistically enhance NH_3 diffusion and uptake.

Based on the collective evidence from the above microscopic characterizations, we also deduce that the mechanism by which acetic acid concentration assists the structure and properties of UiO-66 is rooted in its control over crystallization kinetics. In the absence of HAc, rapid and uncontrolled coordination between Zr clusters and organic linkers results in a densely packed solid with irregular morphology. Interestingly, at the optimal acetic acid concentration (2.5 mL), acetate anions establish a dynamic competitive coordination environment at the Zr nodes. This moderated coordination kinetics promotes the transformation of intergrown crystallites into uniform octahedral microcrystals while simultaneously optimizing interplanar spacing, defect density, and porosity, thus facilitating the targeted synthesis of a structurally superior material [31,32].

3.2. NH_3 adsorption performance

The adsorption rate is a critical metric for assessing gas separation efficiency, directly reflecting the practical applicability of adsorbents [45]. As depicted in Fig. 5a, the NH_3 adsorption rate curves of UiO-66-V (V = 1.0, 2.5, 4.0) MOFs were systematically investigated at 298.2 K and 100 kPa. Remarkably, all HAc-assisted UiO-66-V variants demonstrated significantly enhanced adsorption rates compared to pristine UiO-66. In particular, UiO-66-2.5 achieved adsorption saturation within merely 5 min, whereas pristine UiO-66 required 30 min, representing a 6-fold

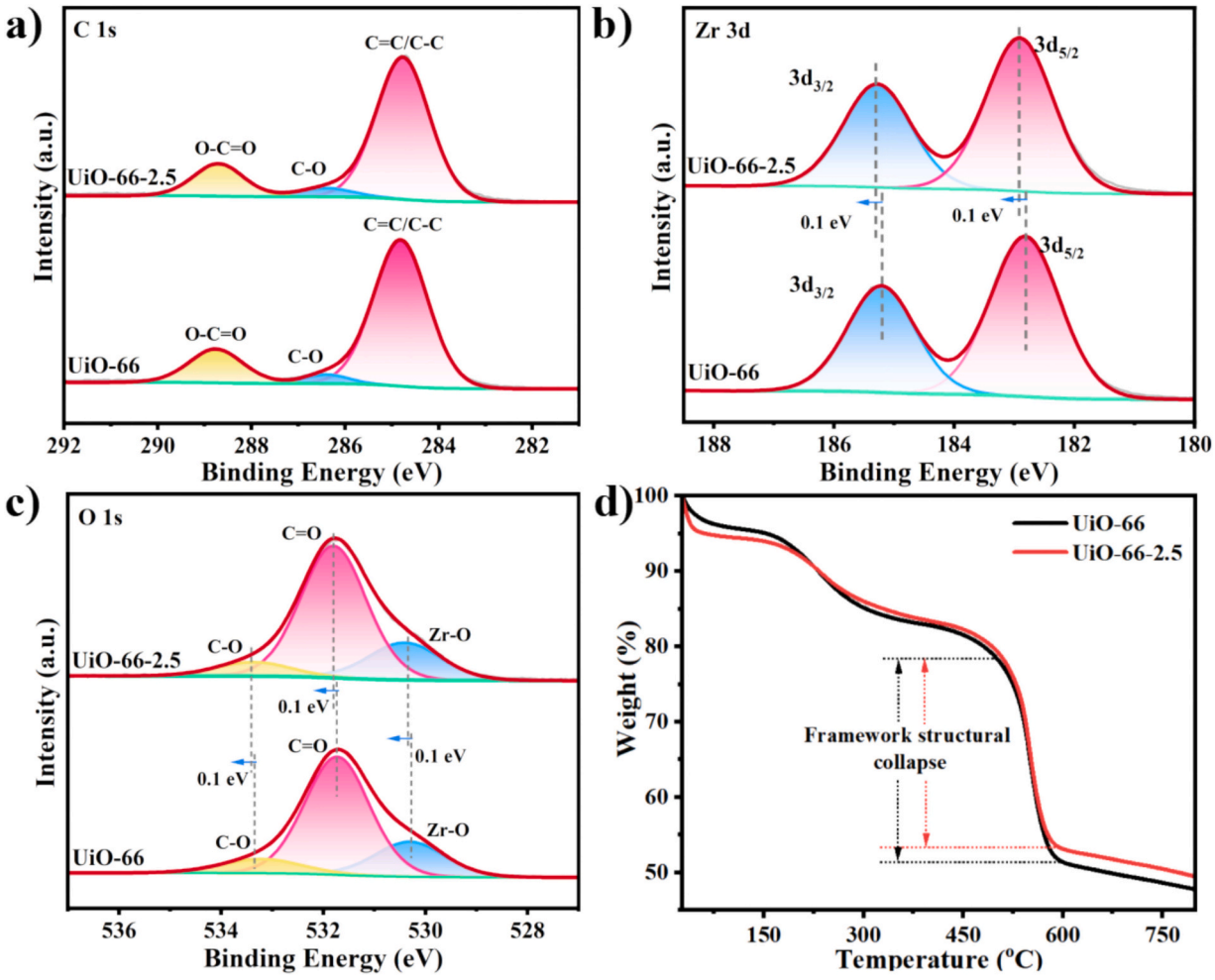

Fig. 4. High-resolution XPS spectra in (a) C 1s, (b) Zr 3d and (c) O 1s and (d) TGA curves of UiO-66 and UiO-66-2.5.

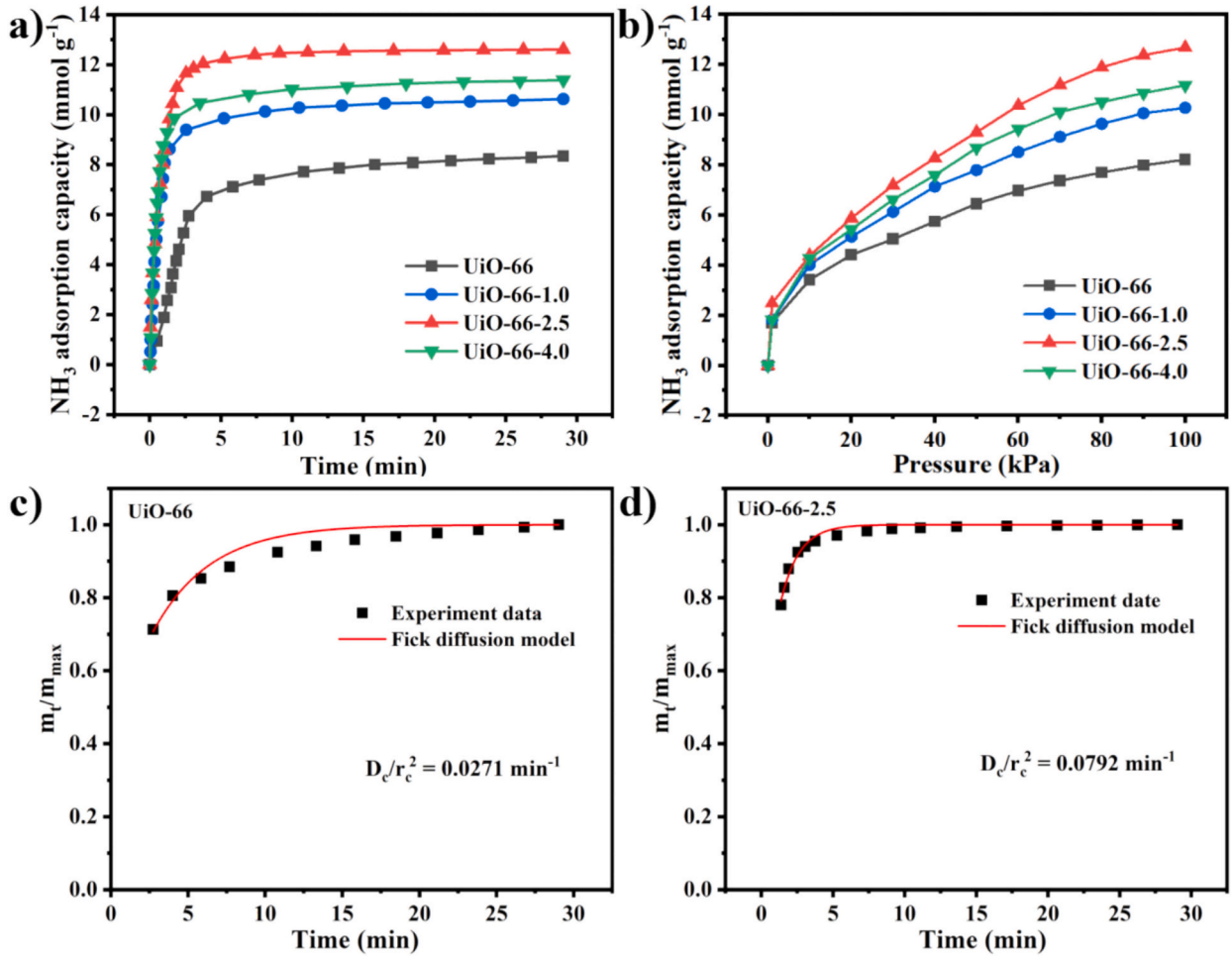

Fig. 5. (a) NH_3 adsorption rate at 298.2 K and 100 kPa and (b) the adsorption isotherms of UiO-66 and UiO-66-V (V = 1.0, 2.5, 4.0) at 298.2 K, (c, d) fitting curves of the Fick diffusion model for UiO-66 and UiO-66-2.5.

enhancement in adsorption rate. The dramatic improvement can be attributed to the strengthened coordinative interaction between Zr sites and NH_3 molecules induced by HAc treatment, which facilitates more efficient mass transfer during the adsorption process [24,29]. Concurrently, the NH_3 adsorption capacities followed the order: UiO-66-2.5 (12.60 mmol g^{-1}) > UiO-66-4.0 (11.38 mmol g^{-1}) > UiO-66-1.0 (10.62 mmol g^{-1}) > pristine UiO-66 (8.34 mmol g^{-1}). The above enhancement correlates well with the substantially increased specific surface area of HAc-treated samples, confirming that the acid-assisted synthesis protocol effectively optimizes NH_3 adsorption performance.

Subsequently, the NH_3 adsorption isotherms of UiO-66 and UiO-66-V (V = 1.0, 2.5, 4.0) at 298.2 K reveal distinct nonlinear uptake profiles (Fig. 5b). The NH_3 adsorption capacity of UiO-66-2.5 quickly increases from 0 to 3.49 mmol g^{-1} in the pressure range of 0–10 kPa, indicating the relatively strong chemisorption interactions between the framework and NH_3 molecules. The pronounced low-pressure adsorption suggests the presence of high-affinity binding sites generated through the HAc assistance process. Furthermore, the adsorption kinetics were further analyzed by fitting the NH_3 adsorption rate curves with the Fick's diffusion model (Fig. 5c and d), which yielded a good fit ($R^2 > 0.90$). The higher diffusion coefficient obtained for UiO-66-2.5 (0.0792 min^{-1}) compared to UiO-66 (0.0271 min^{-1}) demonstrates its faster adsorption

Table 1
Comparison of NH_3 adsorption capacity and rate by UiO-66 and UiO-66-2.5 with representative adsorbents reported in the literatures.

Sample	Temperature (K)	Pressure (bar)	NH_3 uptake capacity (mmol g^{-1})	NH_3 uptake times (min)	NH_3 uptake rate (mmol g^{-1} min^{-1})	Ref.
UiO-66-2.5	298.2	1.0	12.6	7	1.80	This
UiO-66	298.2	1.0	8.34	30	0.28	work
PB/NBC-500-4-4	298.2	1.0	8.99	30	0.30	[45]
PDVB-2.0AA	298.2	1.0	6.91	60	0.07	[46]
PDVB-3.0AA	298.2	1.0	5.03	160	0.03	[46]
$Zn(INA)_2$	298.2	1.0	6	6	1.00	[47]
40 wt% [TEAH][CF_3SO_3]@MCM-41	313.2	1.0	6.62	15	0.44	[48]
MCM-41	313.2	1.0	5.04	25	0.20	[48]
48.89 wt% $[Bmim]_2[Co(SCN)_4]$ @silicagel	303.2	1.0	5.87	15	0.39	[49]
20 wt% [2-Mim][NTf_2]/AC-980	303.2	1.0	4.03	6	0.67	[50]
MOF-253(Al)	298.2	1.0	5.5	90	0.06	[51]

kinetics. In addition, the NH_3 adsorption performances of UiO-66-2.5 and UiO-66 are comprehensively compared with those of the reported adsorbents in literature (Table 1) [45–51]. Notably, the optimal UiO-66-2.5 variant demonstrated a sixfold increase in adsorption rate compared to the pristine UiO-66. The results indicate that the UiO-66-2.5 has satisfactory adsorption capacity and rate for NH_3 capture compared to a majority of reported porous materials.

To further elucidate the NH_3 adsorption behavior of UiO-66 and UiO-66-2.5, their adsorption isotherms were fitted using both the Langmuir and Freundlich models [5]. As shown in Figs. S6, the Freundlich model provides a better fit to the experimental data for both materials compared to the Langmuir model. The correlation coefficients (R^2) of the Freundlich model exceed 0.995 for UiO-66 and 0.998 for UiO-66-2.5, indicating its high accuracy in describing the NH_3 adsorption process. These results suggest that NH_3 molecules are adsorbed onto heterogeneous sites, facilitating multilayer adsorption and the formation of molecular clusters within the micropores of both adsorbents. The adsorption enthalpy was further quantified by fitting the adsorption data using the Clausius-Clapeyron equation (Eqs. (S6) and (S7)) [52,53]. The enthalpy of adsorption ($\Delta_{ads}H$) was derived from the slope of the linear regression of ln p against 1/T at different equilibrium uptake levels (Figs. S6 and S7). The calculated $\Delta_{ads}H$ values are approximately -66 kJ·mol^{-1} for UiO-66-2.5 and -60 kJ·mol^{-1} for pristine UiO-66. The more negative value observed for UiO-66-2.5 indicates a stronger host-guest interaction with NH_3 molecules, which can be ascribed to the increased Lewis acidity generated through acetic acid-assisted synthesis.

3.3. IAST selectivity and breakthrough performance

The selective adsorption of NH_3 from industrial tail gases, which often contain competing species, such as N_2 and H_2, poses a considerable technological challenge. To tackle this issue, we systematically evaluated the gas separation performance of UiO-66-2.5 using comprehensive adsorption measurements. As depicted in Fig. 6a, the single-component adsorption isotherms of NH_3, N_2, and H_2 were measured at 298.2 K and 100 kPa. Notably, UiO-66-2.5 exhibits markedly distinct affinities for these gases, with adsorption capacities of merely 0.104 and 0.016 mmol g^{-1} for N_2 and H_2, respectively, compared to 12.60 mmol g^{-1} for NH_3, highlighting its superior capability for NH_3 recognition. Quantitative analysis via the Ideal Adsorbed Solution Theory (IAST) reveals exceptional separation selectivity of 745 for NH_3/N_2 (3:97 v/v) and 6036 for NH_3/H_2 (3:97 v/v) at 298.2 K and 100 kPa (Fig. 6b). In comparison to the pristine UiO-66, the UiO-66-2.5 maintains high selectivity toward NH_3 in the presence of competitive gases (N_2 and H_2), underscoring the crucial role of HAc assistance in creating selective binding sites for enhanced selective adsorption.

Breakthrough experiments were systematically conducted to evaluate the practical separation performance of UiO-66-2.5 under dynamic flow conditions. Using a simulated industrial gas mixture (3 % NH_3/24.25 % N_2/72.75 % H_2) at 303.2 K and 100 kPa with a flow rate of 25

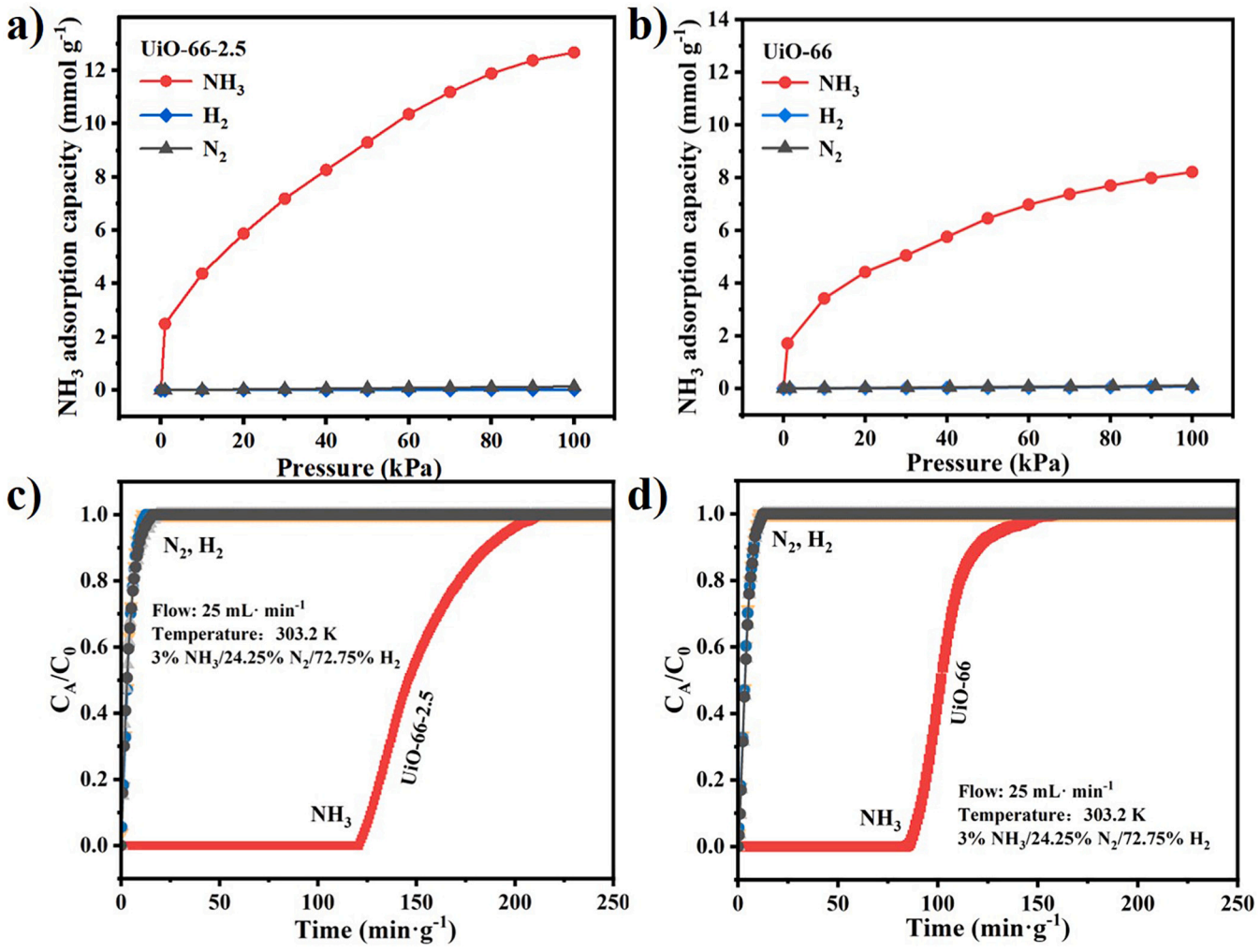

Fig. 6. (a, b) NH_3, N_2, and H_2 uptake isotherms of UiO-66-2.5 and UiO-66 at 298.2 K, 1.0 bar, (c, d) Experimental breakthrough curves of simulated NH_3 flue gas separation by UiO-66-2.5 and UiO-66 at 303.2 K.

mL min^{-1}, UiO-66-2.5 demonstrated exceptional NH_3 capture performance (Fig. 6c and d). The optimized adsorbent exhibited a breakthrough time of 120 min g^{-1}, representing a 42.9 % increase compared to pristine UiO-66 (84 min g^{-1}). Moreover, the dynamic selectivity values for NH_3/H_2 and NH_3/N_2 reached 1725 and 960, respectively, in UiO-66-2.5, significantly higher than those of pristine UiO-66 (675 and 344). These results indicate that HAc-treated UiO-66-2.5 possesses remarkable potential for selectively recovering NH_3 from industrial waste gases.

Notably, the nearly overlapping breakthrough profiles of H_2 and N_2 in both UiO-66-2.5 and the empty column (Fig. 6c and d) clearly indicate the material's negligible affinity toward these competing gases. This attribute allows the direct production of high-purity H_2/N_2 mixtures from the column effluent, which can be readily recycled as feedstock for NH_3 synthesis. The exceptional separation performance stems from the enhanced NH_3 binding affinity at the modified Zr sites and the precisely tailored pore architecture, which collectively promote selective NH_3 diffusion and adsorption.

Besides, the economic feasibility and processability are very important metrics toward large-scale industrialized applications. The cost estimation for UiO-66-2.5 was performed based on laboratory-scale synthesis using commercially available precursors. Besides, the NH_3 adsorption capacity per unit cost was evaluated and compared with that of benchmark adsorbents. As shown in Tables S3 and S4, the cost per gram of NH_3 adsorbed by UiO-66-2.5 is higher than that of activated carbon, it is lower than that of MCM-41. More importantly, the outstanding NH_3 separation and purification capability of UiO-66-2.5 is further demonstrated through breakthrough experiments, in which NH_3 with a purity exceeding 98 % can be efficiently recovered from the separation column, surpassing the performance of conventional activated carbon (30 %) (Fig. S9). This combination of competitive cost and highly selective purification makes UiO-66-2.5 a promising candidate for practical NH_3 separation applications.

3.4. Cycling stability and structural integrity assessment

Cycling stability is a critical parameter governing the long-term practical applicability of adsorbents. As illustrated in Fig. 7a, approximately 92 % of the adsorbed NH_3 was desorbed by regeneration at 353.2 K under vacuum for 2 h. Although a small amount of NH_3 residual was observed, the regenerated adsorbent maintained stable NH_3 uptake capacity throughout the 10 consecutive cycles. In addition, the XRD patterns of both the fresh and regenerated adsorbents confirm that the crystalline structure of UiO-66-2.5 remains largely intact after multiple NH_3 adsorption/desorption cycles, demonstrating remarkable structural robustness (Fig. 7b). Furthermore, the FTIR spectrum of the regenerated UiO-66-2.5 closely matches that of the fresh sample (Fig. S8), providing further evidence of its retained chemical and structural integrity. These results collectively attest to the excellent reusability and stability of UiO-66-2.5, highlighting its promising potential for long-term ammonia recovery from industrial tail gases.

3.5. Adsorption mechanism

To further elucidate the exceptional NH_3 adsorption performance of UiO-66-2.5, the interactions between NH_3 molecules and the MOF framework were investigated using FTIR spectroscopy, temperature-programmed desorption (TPD), and XPS. As shown in Fig. 8a, the Zr 3d XPS spectra of UiO-66-2.5 exhibit two peaks at 182.91 eV and 185.29 eV, corresponding to Zr $3d_{5/2}$ and Zr $3d_{3/2}$ of Zr^{4+} species in the Zr—O bond, respectively. After NH_3 adsorption, these peaks shifted to lower binding energies of 182.85 eV and 185.22 eV, indicating coordination between Zr sites and NH_3 molecules. Additionally, the C═O peak exhibited a noticeable shift from 531.80 eV to 531.74 eV (Fig. 8b), suggesting that carbonyl groups in the framework participate in NH_3 capture via C═O···H-N interactions [54]. In the FTIR spectra (Fig. 8c), the intensity of the peak at 1411 cm^{-1}, attributed to the bending vibration of -OH···H-NH_2, increased significantly, confirming the formation of hydrogen bonds between hydroxyl groups (e.g., from coordinated H_2O) and NH_3. The enhanced intensity of the peak at 3145 cm^{-1}, associated with ν(-OH), further supports the role of hydrogen bonding in NH_3 adsorption [55]. To probe the strength and concentration of Lewis acid sites, NH_3-TPD and pyridine-adsorbed FTIR analyses were conducted on both UiO-66-2.5 and pristine UiO-66. The NH_3-TPD profiles (Fig. 8d) show that both adsorbents exhibit similar NH_3 desorption behaviors at 90–110 °C. Notably, a new and broad NH_3 desorption peak centered at 191.2 °C appears uniquely in the profile of UiO-66-2.5, indicating the presence of stronger acid sites in the acetic acid-assisted material [56]. Furthermore, as shown in Fig. S10, the characteristic bands at 1437 cm^{-1} and 1578 cm^{-1}, which are attributed to pyridine coordinated to Lewis acid sites [57]. The peak areas of Lewis acids sites for UiO-66-2.5 are larger than those of the pristine UiO-66 in FTIR spectra, confirming a higher concentration of Lewis acid sites [58].

Furthermore, the exceptional NH_3 separation performance of UiO-66-2.5 is attributed to a synergistic mechanism combining optimized pore architecture and enhanced surface chemistry. The acetic acid-assisted synthesis yields a well-defined micropore system, where larger micropores serve as diffusion pathways, reducing mass transfer resistance and enabling rapid access of NH_3 molecules to adsorption sites, while smaller micropores provide high surface area and host a high density of open Zr sites. The sites exhibit strong affinity toward NH_3 via Lewis acid-base interactions, leading to high adsorption selectivity. The cooperation between efficient molecular transport and strong specific binding ensures high dynamic capacity and stable cyclic performance.

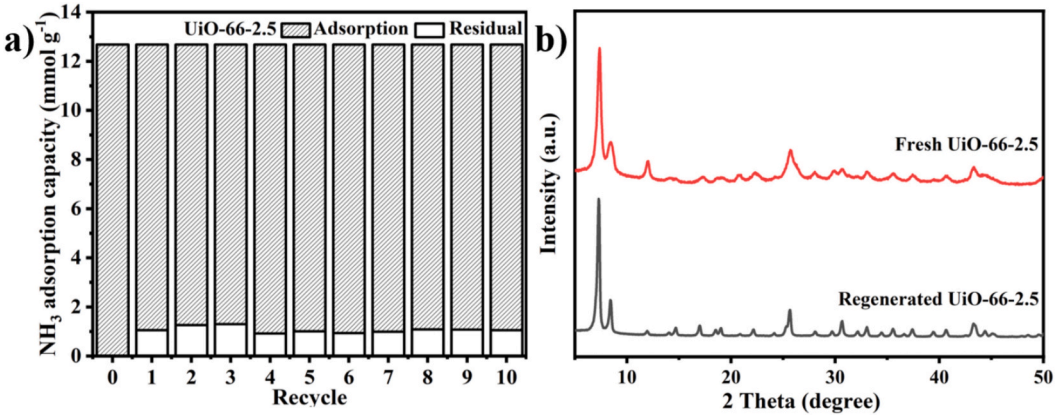

Fig. 7. (a) Regeneration performance of UiO-66-2.5 for NH_3 adsorption at 298.2 K, (b) XRD patterns of fresh UiO-66-2.5 and regenerated UiO-66-2.5.

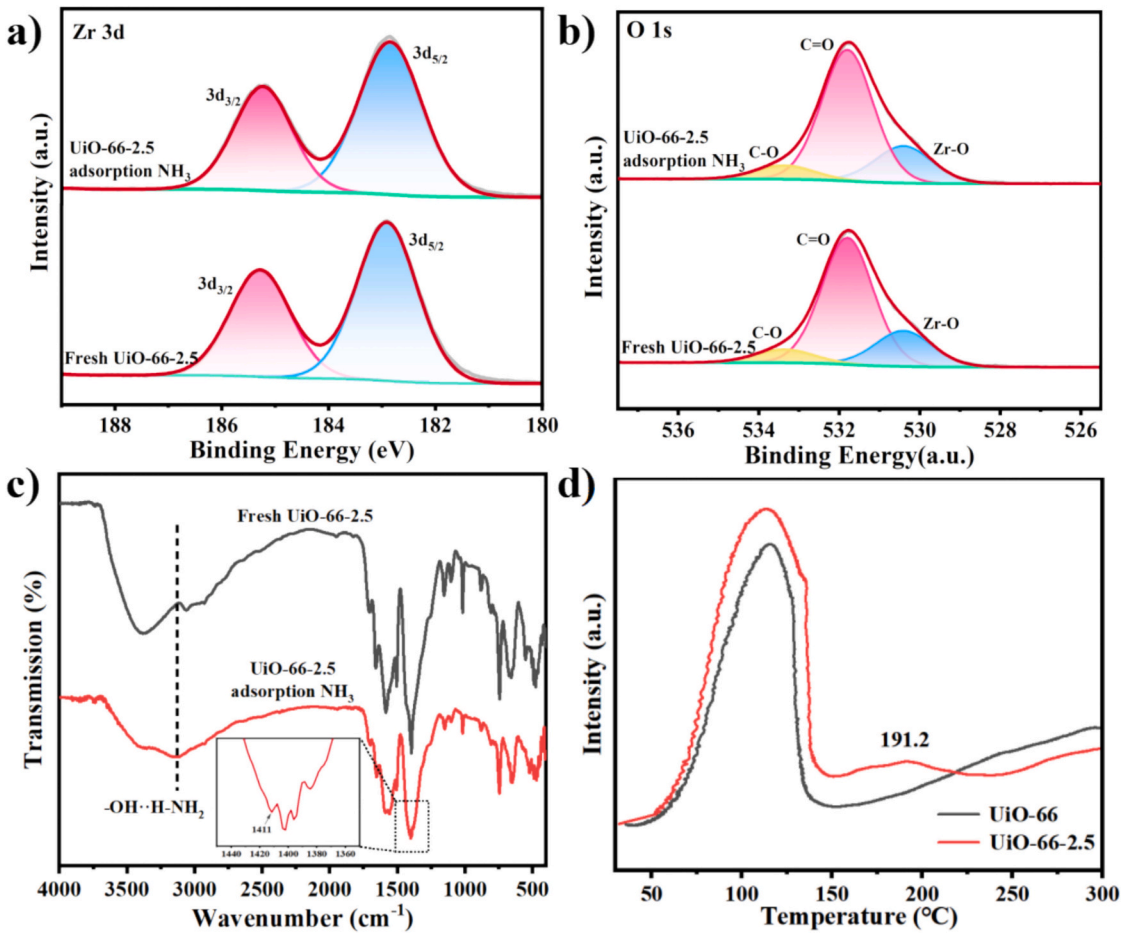

Fig. 8. XPS spectra of (a) Zr 3d, (b) O 1s and (c) FTIR spectra of fresh UiO-66-2.5 and UiO-66-2.5 adsorption NH_3 (d) NH_3-TPD curves of UiO-66 and UiO-66-2.5.

3.6. Pelletization and industrial feasibility assessment

To evaluate the industrial applicability of UiO-66-2.5, we conducted systematic pelletization studies. Mechanical stability of the resulting 90 % UiO-66-2.5@PVA, 90 % UiO-66-2.5@HEC and 90 % UiO-66-2.5@CMC pellets was assessed through compressive stress and abrasion tests, performed with a compression testing machine and planetary ball mill, respectively (Fig. 9a and b). Among the three binder systems, PVA-bound pellets exhibited superior mechanical integrity, demonstrating a compressive strength of 97.19 N and a minimal mass loss of only 1.70 % after abrasion testing at 200 rpm for 2 h. These findings confirm that the 90 % UiO-66-2.5@PVA pellets possess outstanding mechanical robustness and abrasion resistance, essential for maintaining structural integrity during industrial handling and operation. Since pressure drop is inversely proportional to particle size, the bed pressure drop of 90 % UiO-66-2.5 pellets is lower than that of UiO-66-2.5 powders, which is consistent with the reported literature [59].

Then, as presented in Fig. 9c, the adsorption rates of UiO-66-2.5 adsorbent powder and pellets (90 %UiO-66-2.5@PVA, 90 %UiO-66-2.5@HEC, and 90 %UiO-66-2.5@CMC) were investigated. All three types of pellets maintained rapid adsorption rates and high adsorption capacity retention. Notably, the 90 % UiO-66-2.5@PVA pellets reached 92.6 % of the saturation capacity within 3 min. It is worth noting that the PVA binder itself exhibits negligible NH_3 adsorption capacity (Fig. S11), confirming that the adsorption performance of the granules is predominantly attributable to the UiO-66-2.5 component. Furthermore, dynamic breakthrough experiments were conducted to evaluate the separation performance under realistic conditions (Fig. 9d). The 90 % UiO-66-2.5@PVA pellets exhibited a breakthrough time of 100 $min \cdot g^{-1}$ for a $NH_3/N_2/H_2$ mixture (3/24.25/72.75, v/v/v), which is comparable to that (120 $min \cdot g^{-1}$) of the UiO-66-2.5 powder. This slight performance reduction is attributed to the increased density of the pelletized form, which reduces the external contact area with the gas stream and slightly elevates mass transfer resistance [5,6]. Importantly, the pelletization process did not significantly block the porous structure or cover active sites, thereby preserving the intrinsic separation functionality of UiO-66-2.5. In summary, the UiO-66-2.5 material retains high separation performance and mechanical robustness after pelletization.

4. Conclusion

In summary, we have successfully developed a series of HAc-assisted UiO-66-V adsorbents for highly efficient capture of low-concentration NH_3. The optimized UiO-66-2.5 material exhibits significantly enhanced textural properties and Lewis acidity, leading to exceptional NH_3 adsorption capacity, outstanding selectivity, and excellent recyclability. Notably, UiO-66-2.5 achieves an NH_3 adsorption rate six times higher than that of pristine UiO-66, along with exceptional IAST selectivities of 745 for NH_3/N_2 (3:97) and 6036 for NH_3/H_2 (3:97) at 298.2 K and 1.0 bar. Breakthrough experiments further demonstrate superior dynamic separation performance, with a retention time of 120 min g^{-1} for a simulated industrial gas mixture, surpassing the pristine material (84 min g^{-1}). Moreover, the adsorbent retains 92 % of its initial capacity after 10 consecutive adsorption-desorption cycles, underscoring its remarkable structural integrity and regeneration capability. These results collectively demonstrate that acid-assisted synthesis is an effective strategy for designing MOFs adsorbents with balanced capacity, kinetics, and stability suited for industrial NH_3 capture.

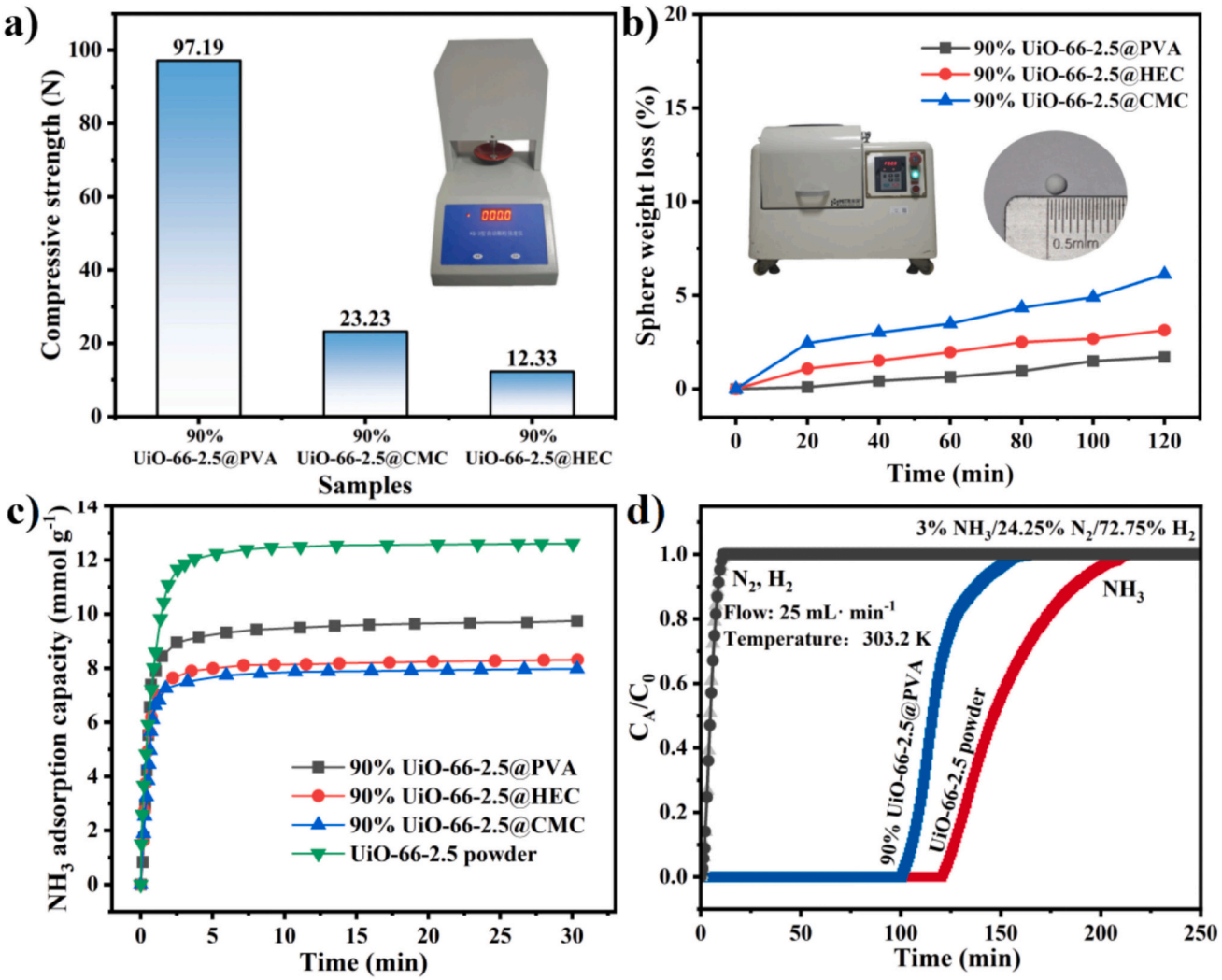

Fig. 9. (a) Compressive strength, (b) the wear test, (c) NH3 adsorption rate of 90 % UiO-66-2.5@ PVA, 90 % UiO-66-2.5@HEC and 90 % UiO-66-2.5@CMC, (d) experimental breakthrough curves of simulated NH_3 flue gas separation by 90 % UiO-66-2.5@PVA and UiO-66-2.5 powder.

CRediT authorship contribution statement

Jia-Hui Chen: Writing – original draft, Validation, Methodology, Investigation, Formal analysis, Conceptualization. **Hao-Yu Jiang:** Writing – original draft, Methodology, Investigation, Formal analysis, Conceptualization. **Wen-Qiang Gong:** Writing – original draft, Methodology, Conceptualization. **Wei Hui:** Visualization, Validation, Funding acquisition, Formal analysis, Data curation. **Xiao-Liang Zhang:** Validation, Resources, Methodology, Funding acquisition. **Ming-Shuai Sun:** Methodology, Investigation, Formal analysis. **Dan-Dan Cai:** Writing – review & editing, Writing – original draft, Supervision, Resources, Project administration, Investigation, Funding acquisition. **Duan-Jian Tao:** Writing – review & editing, Supervision, Project administration, Investigation, Funding acquisition.

Declaration of competing interest

The authors declare that they have no known competing financial interests or personal relationships that could have appeared to influence the work reported in this paper.

Acknowledgements

We thank the National Natural Science Foundation of China (22378178, 22508154), Jiangxi Provincial Natural Science Foundation (20252BAC240292, 20242BAB20111, 20232ACB203020) for the financial support.

Appendix A. Supplementary data

Supplementary data to this article can be found online at https://doi.org/10.1016/j.cej.2025.170580.

Data availability

No data was used for the research described in the article.

References

[1] H.Y. Jiang, Z.M. Wang, X.Q. Sun, S.J. Zeng, Y.Y. Guo, L. Bai, M.S. Yao, X.P. Zhang, Advanced materials for NH_3 capture: interaction sites and transport pathways, Nano-Micro Lett. 16 (2024) 228.
[2] J.W. Erisman, How ammonia feeds and pollutes the world, Science 374 (2021) 685–686.
[3] R. Luo, D. Xu, R. Liu, J. Zhou, X. Ma, Metal-organic frameworks for NH_3 adsorption and separation, Nanoscale 17 (2025) 13561–13580.
[4] J. Zhang, L. Zheng, Y. Ma, Z. Cai, Y. Cao, K. Huang, L. Jiang, A mini-review on NH_3 separation technologies: recent advances and future directions, Energ, Fuel 36 (2022) 14516–14533.

[5] G. Fang, Z. Li, J. Li, D. Cai, Y. Xiong, Y. Zhou, W. Hui, D. Tao, Waste lignosulfonate upcycling towards durable and efficient pelletized adsorbents for diluted NH_3 adsorption, Chem. Eng. J. 507 (2025) 160639.

[6] W. Gong, Y. Fu, Y. Zhou, M. Sun, Z. Li, N. Lu, D. Tao, Efficient cavity-enhanced adsorption and recovery of low-concentration ammonia on pillar[5]arenes, Sep. Purif. Technol. 322 (2023) 124304.

[7] J. Zhang, S. Fang, L. Zheng, Y. Cao, H. Zhang, Z. Cai, K. Huang, L. Jiang, Mesoporous polymer supported metal-based deep eutectic solvents for enhanced capture of low-content ammonia, Chem. Eng. J. 493 (2024) 152562.

[8] T. Islamoglu, Z. Chen, M.C. Wasson, C.T. Buru, K.O. Kirlikovali, U. Afrin, M. R. Mian, O.K. Farha, Metal-organic frameworks against toxic chemicals, Chem. Rev. 120 (2020) 8130–8160.

[9] Y. He, B. Guan, Z. Zhuang, J. Chen, L. Zhu, Z. Ma, X. Hu, C. Zhu, S. Zhao, K. Shu, H. Dang, T. Zhu, Z. Huang, Advances in ammonia (NH_3) adsorption and storage: materials, mechanisms, and applications, Adsorption 31 (2025) 48.

[10] X. Han, W. Lu, Y. Chen, I. da Silva, J. Li, L. Lin, W. Li, A.M. Sheveleva, H.G. W. Godfrey, Z. Lu, F. Tuna, E.J.L. McInnes, Y. Cheng, L.L. Daemen, L.J. M. McPherson, S.J. Teat, M.D. Frogley, S. Rudic, P. Manuel, A.J. Ramirez-Cuesta, S. Yang, M. Schroder, High ammonia adsorption in MCM-300 materials: dynamics and charge transfer in host-guest binding, J. Am. Chem. Soc. 143 (2021) 3153–3161.

[11] W. Lu, D. De Alwis Jayasinghe, M. Schroder, S. Yang, Ammonia storage in metal-organic framework materials: recent developments in design and characterization, Acc. Mater. Res. 5 (2024) 1279–1290.

[12] B.E.R. Snyder, A.B. Turkiewicz, H. Furukawa, M.V. Paley, E.O. Velasquez, M. N. Dods, J.R. Long, A ligand insertion mechanism for cooperative NH_3 capture in metal-organic frameworks, Nature 613 (2023) 287–291.

[13] C. Marsh, X. Han, J. Li, Z. Lu, S.P. Argent, I. da Silva, Y. Cheng, L.L. Daemen, A. J. Ramirez-Cuesta, S.P. Thompson, A.J. Blake, S. Yang, M. Schroder, Exceptional packing density of ammonia in a dual-functionalized metal-organic framework, J. Am. Chem. Soc. 143 (2021) 6586–6592.

[14] D.W. Kim, D.W. Kang, M. Kang, D.S. Choi, H. Yun, S.Y. Kim, S.M. Lee, J.H. Lee, C. S. Hong, High gravimetric and volumetric ammonia capacities in robust metal-organic frameworks prepared via double postsynthetic modification, J. Am. Chem. Soc. 144 (2022) 9672–9683.

[15] J.F. Kurisingal, N. Kim, D.W. Kim, H. Yun, C.S. Hong, Metal-organic frameworks and composites for ammonia capture, Small 21 (2025) 2503970.

[16] A.J. Rieth, M. Dinca, Controlled gas uptake in metal-organic frameworks with record ammonia sorption, J. Am. Chem. Soc. 140 (2018) 3461–3466.

[17] L.N. McHugh, A. Terracina, P.S. Wheatley, G. Buscarino, M.W. Smith, R.E. Morris, Metal-organic framework-activated carbon composite materials for the removal of ammonia from contaminated airstreams, Angew. Chem. Int. Ed. 58 (2019) 11747–11751.

[18] D.W. Kim, D.W. Kang, M. Kang, J.H. Lee, J.H. Choe, Y.S. Chae, D.S. Choi, H. Yun, C.S. Hong, High ammonia uptake of a metal-organic framework adsorbent in a wide pressure range, Angew. Chem. Int. Ed. 59 (2020) 22531–22536.

[19] J. Liu, Z. Chen, R. Wang, S. Alayoglu, T. Islamoglu, S.J. Lee, T.R. Sheridan, H. Chen, R.Q. Snurr, O.K. Farha, J.T. Hupp, Zirconium metal–organic frameworks integrating chloride ions for ammonia capture and/or chemical separation, ACS Appl. Mater. Interfaces 13 (2021) 22485–22494.

[20] Y. Wang, Y. Shi, Z. Li, H. Wang, J. Qiu, X. Xuan, J. Wang, Defects in a metal–organic framework fabricated by carboxy-functionalized ionic liquids for enhancing NH_3 uptake, ACS Sustain. Chem. Eng. 10 (2022) 12457–12465.

[21] J.N. Joshi, E.Y. Garcia-Gutierrez, C.M. Moran, J.I. Deneff, K.S. Walton, Engineering copper carboxylate functionalities on water stable metal-organic frameworks for enhancement of ammonia removal capacities, J. Phys. Chem. C 121 (2017) 3310–3319.

[22] H. Wu, Y.S. Chua, V. Krungleviciute, M. Tyagi, P. Chen, T. Yildirim, W. Zhou, Unusual and highly tunable missing-linker defects in zirconium metal–organic framework UiO-66 and their important effects on gas adsorption, J. Am. Chem. Soc. 135 (2013) 10525–10532.

[23] E. Binaeian, Y. Li, D. Yuan, Improving ammonia uptake performance of zirconium-based metal-organic frameworks through open metal site insertion strategy, Chem. Eng. J. 421 (2021) 129655.

[24] Y. Ma, W. Lu, X. Han, Y. Chen, I. da Silva, D. Lee, A.M. Sheveleva, Z. Wang, J. Li, W. Li, M. Fan, S. Xu, F. Tuna, E.J.L. McInnes, Y. Cheng, S. Rudić, P. Manuel, M. D. Frogley, A.J. Ramirez-Cuesta, M. Schröder, S. Yang, Direct observation of ammonia storage in UiO-66 incorporating Cu(II) binding sites, J. Am. Chem. Soc. 144 (2022) 8624–8632.

[25] A. Schaate, P. Roy, A. Godt, J. Lippke, F. Waltz, M. Wiebcke, P. Behrens, Modulated synthesis of Zr-based metal-organic frameworks: from nano to single crystals, Chem. Eur. J. 17 (2011) 6643–6651.

[26] F. Vermoortele, B. Bueken, G. Le Bars, B. Van de Voorde, M. Vandichel, K. Houthoofd, A. Vimont, M. Daturi, M. Waroquier, V. Van Speybroeck, C. Kirschhock, D.E. De Vos, Synthesis modulation as a tool to increase the catalytic activity of metal-organic frameworks: the unique case of UiO-66(Zr), J. Am. Chem. Soc. 135 (2013) 11465–11468.

[27] J. Ren, H.W. Langmi, B.C. North, M. Mathe, D. Bessarabov, Modulated synthesis of zirconium-metal organic framework (Zr-MOF) for hydrogen storage applications, Int. J. Hydrog. Energy 39 (2014) 890–895.

[28] E. Binaeian, Y. Li, H. Tayebi, D. Yuan, Enhancing toxic gas uptake performance of Zr-based mof through uncoordinated carboxylate and copper insertion; ammonia adsorption, J. Hazard. Mater. 416 (2021) 125933.

[29] T. Yoskamtorn, P. Zhao, X. Wu, K. Purchase, F. Orlandi, P. Manuel, J. Taylor, Y. Li, S. Day, L. Ye, C.C. Tang, Y. Zhao, S.C.E. Tsang, Responses of defect-rich Zr-based metal-organic frameworks toward NH_3 adsorption, J. Am. Chem. Soc. 143 (2021) 3205–3218.

[30] M. Khanpour Matikolaei, E. Binaeian, Boosting ammonia uptake within metal–organic frameworks by anion modulating strategy, ACS Appl. Mater. Interfaces 13 (2021) 27159–27168.

[31] G.C. Shearer, S. Chavan, S. Bordiga, S. Svelle, U. Olsbye, K.P. Lillerud, Defect engineering: tuning the porosity and composition of the metal–organic framework UiO-66 via modulated synthesis, Chem. Mater. 28 (2016) 3749–3761.

[32] Y. Zhao, Q. Zhang, Y. Li, R. Zhang, G. Lu, Large-scale synthesis of monodisperse UiO-66 crystals with tunable sizes and missing linker defects via acid/base co-modulation, ACS Appl. Mater. Interfaces 9 (2017) 15079–15085.

[33] A. Koutsianos, E. Kazimierska, A.R. Barron, M. Taddei, E. Andreoli, A new approach to enhancing the CO_2 capture performance of defective UiO-66 via post-synthetic defect exchange, Dalton Trans. 48 (2019) 3349–3359.

[34] C.J. Doonan, D.J. Tranchemontagne, T.G. Glover, J.R. Hunt, O.M. Yaghi, Exceptional ammonia uptake by a covalent organic framework, Nat. Chem. 2 (2010) 235–238.

[35] B.M. Connolly, D.G. Madden, A.E.H. Wheatley, D. Fairen-Jimenez, Shaping the future of fuel: monolithic metal–organic frameworks for high-density gas storage, J. Am. Chem. Soc. 142 (2020) 8541–8549.

[36] L. He, Z. Yang, X. Lu, Y. Xu, X. Yao, C. Li, C. Wu, Z. Yao, Defective UiO-66 by metal doping for highly efficient photocatalytic degradation of methyl mercaptan, J. Environ. Chem. Eng. 11 (2023) 111419.

[37] J. Li, Z. Li, J. Xu, C.-Y. Guo, G. Fang, Y. Zhou, M. Sun, D. Tao, Demethylation of waste alkali lignin for rapid and efficient ammonia adsorption, Ind. Eng. Chem. Res. 63 (2024) 3282–3289.

[38] Y. Ma, X. Han, S. Xu, Z. Wang, W. Li, I. da Silva, S. Chansai, D. Lee, Y. Zou, M. Nikiel, P. Manuel, A.M. Sheveleva, F. Tuna, E.J.L. McInnes, Y. Cheng, S. Rudić, A.J. Ramirez-Cuesta, S.J. Haigh, C. Hardacre, M. Schröder, S. Yang, Atomically dispersed copper sites in a metal–organic framework for reduction of nitrogen dioxide, J. Am. Chem. Soc. 143 (2021) 10977–10985.

[39] A. Vodyashkin, A. Sergorodceva, P. Kezimana, M. Morozova, E. Nikolskaya, M. Mollaeva, N. Yabbarov, M. Sokol, M. Chirkina, L. Butusov, A. Timofeev, Synthesis and activation of pH-sensitive metal–organic framework Sr(BDC)∞ for oral drug delivery, Dalton Trans. 53 (2024) 1048–1057.

[40] Z. Guo, Z. Liu, K. Zhang, W. Wang, J. Pang, Z. Li, Z. Kang, D. Zhao, Stable metal-organic frameworks based mixed matrix membranes for ethylbenzene/N_2 separation, Chem. Eng. J. 416 (2021) 129193.

[41] G. Yu, F. Ni, W. Niu, Y. Chen, F. Zhang, G. Li, X. Song, Y. Zhang, K. Wang, Precise manipulation of pore sizes in Zr(IV)-based metal-organic frameworks for enhanced bisphenol a removal from water, Chemosphere 369 (2024) 143816.

[42] L. Cheng, D. Cai, Y. He, S. Geng, Y. Wang, S. Song, Toward high corrosion resistivity and high efficiency in seawater oxygen evolution: the synergy of Fe and Ni dopants in co layered double hydroxide ultrathin nanosheets, ACS Sustain. Chem. Eng. 12 (2024) 16365–16377.

[43] F. Li, S. Yun, L. Gui, Y. Zhou, Hydrazino-containing Zr-MOF for enhanced Lewis acid-base catalysis of CO_2 fixation into cyclocarbonate, J. Environ. Chem. Eng. 12 (2024) 114311.

[44] X. Wang, X. Zhang, Y. Zhao, D. Luo, L. Shui, Y. Li, G. Ma, Y. Zhu, Y. Zhang, G. Zhou, A. Yu, Z. Chen, Accelerated multi-step sulfur redox reactions in lithium-sulfur batteries enabled by dual defects in metal-organic framework-based catalysts, Angew. Chem. Int. Ed. 62 (2023) e202306901.

[45] J. Xiao, Y. Zhang, T.C. Zhang, S. Yuan, Prussian blue-impregnated waste pomelo peels-derived biochar for enhanced adsorption of NH_3, J. Clean. Prod. 382 (2023) 135393.

[46] J. Zhang, Y. Ma, W. Wu, Z. Cai, Y. Cao, K. Huang, L. Jiang, Carboxylic functionalized mesoporous polymers for fast, highly efficient, selective and reversible adsorption of ammonia, Chem. Eng. J. 448 (2022) 137640.

[47] Y. Chen, C. Yang, X. Wang, J. Yang, K. Ouyang, J. Li, Kinetically controlled ammonia vapor diffusion synthesis of a Zn(II) MOF and its H_2O/NH_3 adsorption properties, J. Mater. Chem. A 4 (2016) 10345–10351.

[48] S. Zheng, Q. Xu, S. Zeng, G. Li, H. Jiang, X. Sun, X. Zhang, Porous multi-site ionic liquid composites for superior selective and reversible adsorption of ammonia, Sep. Purif. Technol. 310 (2023) 123161.

[49] S. Zeng, J. Wang, P. Li, H. Dong, H. Wang, X. Zhang, X. Zhang, Efficient adsorption of ammonia by incorporation of metal ionic liquids into silica gels as mesoporous composites, Chem. Eng. J. 370 (2019) 81–88.

[50] M. Yu, S. Zeng, Z. Wang, Z. Hu, H. Dong, Y. Nie, B. Ren, X. Zhang, Protic ionic-liquid-supported activated carbon with hierarchical pores for efficient NH_3 adsorption, ACS Sustain. Chem. Eng. 7 (2019) 11769–11777.

[51] Y. Wang, Y. Shi, D. Xiong, Z. Li, H. Wang, X. Xuan, J. Wang, Metal chloride functionalized MOF-253(Al) for high-efficiency selective separation of ammonia from H_2 and N_2, Chem. Eng. J. 474 (2023) 145307.

[52] E.W. Knight, A.K. Gillespie, M.J. Prosniewski, D. Stalla, E. Dohnke, T.A. Rash, P. Pfeifer, C. Wexler, Determination of the enthalpy of adsorption of hydrogen in activated carbon at room temperature, Int. J. Hydrog. Energy 45 (2020) 15541–15552.

[53] A. Nuhnen, C. Janiak, A practical guide to calculate the isosteric heat/enthalpy of adsorption via adsorption isotherms in metal–organic frameworks, MOFs, Dalton Trans. 49 (2020) 10295–10307.

[54] Z. Wang, Z. Li, H. Wang, Y. Zhao, Q. Xia, J. Qiu, J. Wang, Regulating the pore microenvironment of microporous metal-organic frameworks for efficient adsorption of low-concentration ammonia, ACS Sustain. Chem. Eng. 10 (2022) 10945–10954.

[55] G. Han, C. Liu, Q. Yang, D. Liu, C. Zhong, Construction of stable IL@MOF composite with multiple adsorption sites for efficient ammonia capture from dry and humid conditions, Chem. Eng. J. 401 (2020) 126106.
[56] R. Liu, Y. Bian, W. Dai, Qualitative and quantitative analysis of Brønsted and Lewis acid sites in zeolites: a combined probe-assisted ^{1}H MAS NMR and NH_3-TPD investigation, Chin. J. Struct. Chem. 43 (2024) 100250.
[57] Z. Wang, M. Yao, X. Niu, Y. Zhu, Excellent low-temperature activity and resistance to K-poisoning in NH_3-SCR de-NO_x reaction over $CeSnO_x$ with phosphorylation treatment catalyst, Appl. Catal. B Environ. 359 (2024) 124464.
[58] H. Lin, X. Sun, Y. Jin, Y. Yu, Y. Liu, Ammonia-assisted dry-gel conversion for preparation of TS-1 with enriched $Ti(OSi)_3OH$ active sites, Microporous Mesoporous Mater. 390 (2025) 113595.
[59] J. Li, Y. Chen, T. Ke, Y. Jin, R. Fan, G. Xu, L. Yang, Z. Zhang, Z. Bao, Q. Ren, Q. Yang, Efficient continuous SF_6/N_2 separation using low-cost and robust metal-organic frameworks composites, Nat. Commun. 16 (2025) 632.